Journal of Geophysical Research: Atmospheres

Key Points:
- Complex relationship between boundary conditions and ENSO-like expressions
- Mid-Holocene response to ENSO-like forcing is muted in hydrological cycle
- Proxy reconstructions should consider possible nonstationary teleconnections

Supporting Information:
- Readme
- Figure S1
- Figure S2
- Text S1

Correspondence to:
S. C. Lewis,
sophie.lewis@unimelb.edu.au

Comparison of forced ENSO-like hydrological expressions in simulations of the preindustrial and mid-Holocene

Sophie C. Lewis[1,2], Allegra N. LeGrande[3], Gavin A. Schmidt[3], and Maxwell Kelley[3]

[1]School of Earth Sciences, University of Melbourne, Parkville, Victoria, Australia, [2]ARC Centre of Excellence for Climate System Science, Canberra, ACT, Australia, [3]NASA Goddard Institute for Space Studies and Center for Climate Systems Research, Columbia University, New York, New York, USA

Abstract Using the water isotope- and vapor source distribution (VSD) tracer-enabled Goddard Institute for Space Studies ModelE-R, we examine changing El Niño–Southern Oscillation (ENSO)-like expressions in the hydrological cycle in a suite of model experiments. We apply strong surface temperature anomalies associated with composite observed El Niño and La Niña events as surface boundary conditions to preindustrial and mid-Holocene model experiments in order to investigate ENSO-like expressions in the hydrological cycle under varying boundary conditions. We find distinct simulated hydrological anomalies associated with El Niño-like ("$ENSO_{WARM}$") and La Niña-like ("$ENSO_{COOL}$") conditions, and the region-specific VSD tracers show hydrological differences across the Pacific basin between El Niño-like and La Niña-like events. The application of $ENSO_{COOL}$ forcings does not produce climatological anomalies that represent the equal but opposite impacts of the $ENSO_{WARM}$ experiment, as the isotopic anomalies associated with $ENSO_{WARM}$ conditions are generally stronger than with $ENSO_{COOL}$ and the spatial patterns of change distinct. Also, when the same ENSO-like surface temperature anomalies are imposed on the mid-Holocene, the hydrological response is muted, relative to the preindustrial. Mid-Holocene changes in moisture sources to the analyzed regions across the Pacific reveal potentially complex relationships between ENSO-like conditions and boundary conditions. Given the complex impacts of ENSO-like conditions on various aspects of the hydrological cycle, we suggest that proxy record insights into paleo-ENSO variability are most likely to be robust when synthesized from a network of many spatially diverse archives, which can account for the potential nonstationarity of ENSO teleconnections under different boundary conditions.

1. Introduction

The El Niño–Southern Oscillation (ENSO) is characterized by sea surface temperature (SST) anomalies in the tropical Pacific that influence remote rainfall through atmospheric teleconnections and dominate climatic variability in many regions. The strength of remote ENSO teleconnections (i.e., the relative influence of a remote climatic mechanism on regional and local climates) is dependent on changes in the large-scale state of the coupled ocean-atmosphere system [*Gallant et al.*, 2013], and potential changes in the amplitude, length, and frequency of ENSO events under future-changing boundary conditions remain poorly constrained [*Collins et al.*, 2010]. In this present study, we investigate expressions of ENSO-like climatic modes in the hydrological cycle using a global climate model (GCM). As substantially different ENSO expressions may exist in the hydrological cycle under different orbital forcings, we examine the relationship between boundary conditions and changes in the hydrological cycle under ENSO-like forcings using the preindustrial and the mid-Holocene as research targets that characterize distinct background climatic states.

1.1. Proxy $\delta^{18}O$ Reconstructions

Paleoclimatic studies can provide a long-term context for understanding varying ENSO expressions [*Jones and Mann*, 2004; *Gergis et al.*, 2006], although there remain obstacles to increasing our understanding of ENSO variability through both paleoarchives and model-based approaches. First, precisely dated, well-resolved, readily interpretable proxy records are limited. While oxygen isotope ($\delta^{18}O$, δ in permil units, ‰, of the subscripted value relative to a known standard) archives can provide high temporal resolution records from ENSO-impacted areas [*Cobb et al.*, 2003, 2013], proxy $\delta^{18}O$ is often dependent on multiple, complex climatic $\delta^{18}O$. Coral $\delta^{18}O$ responds to water temperature changes together with rainfall variability, due to the influence of isotopically depleted rainfall on surface ocean composition [*Tudhope et al.*, 2001]. Speleothem

and ice core-based δ^{18}O records provide complementary climatic archives [*Lachniet et al.*, 2004], but these may integrate changes in temperature or precipitation, together with vapor source due to circulation changes [*Vuille et al.*, 2003].

In addition, the nonstationary nature of ENSO teleconnections can limit the utility of proxy-derived ENSO reconstructions [*Gallant et al.*, 2013]. As the spatial influence of ENSO likely changes under different boundary conditions, preserved climatic signals may become convoluted [*Wilson et al.*, 2010] and interpolating climatic conditions from local reconstructions to basin-wide generalizations may be spurious [*Rosenthal and Broccoli*, 2004]. Hence, multiproxy data from many widely spaced regional proxies are most useful for obtaining precise information of temporal changes in large-scale ocean-atmosphere processes [e.g., *Emile-Geay et al.*, 2012]. Overall, ENSO-sensitive proxy records indicate distinct changes in the nature of teleconnection patterns, together with differences in ENSO amplitude, frequency, and length compared to the present day [e.g., *Tudhope et al.*, 2001; *Bush*, 2007; *McGregor et al.*, 2013a].

1.2. Previous Modeling Work

Global climate models provide an additional tool for understanding ENSO variability on longer timescales and also for understanding how δ^{18}O archives record climatic variability [*Toniazzo*, 2006; *Brown et al.*, 2008; *Chiang et al.*, 2009; *Conroy et al.*, 2013]. As both the climatic mean state and dynamics of the coupled ocean-atmosphere ENSO system in the tropical Pacific were likely different in the mid-Holocene compared with present day, this provides a useful period to examine changes in the ENSO system [*Luan et al.*, 2012]. Previous model-based studies indicate that ENSO is sensitive to the orbital variations, and the dynamical interaction between the tropical atmosphere and oceans is particularly influenced by precessional modulation of the seasonal cycle [*Clement et al.*, 1999]. A reduction in ENSO amplitude in the mid-Holocene arises from changes in seasonality that influences the depth and intensity of the thermocline and the timing of the development of ENSO associated [*Luan et al.*, 2012].

Modeling analyses that explicitly incorporate water isotope tracers also move us closer to making comparisons between proxy records and model data [*Brown et al.*, 2006, 2008; *Schmidt et al.*, 2007]. Water isotope tracer analyses have helped constrain δ^{18}O anomalies associated with modern ENSO conditions and determined regions where simulated δ^{18}O$_p$ is significantly correlated with ENSO variability [*Vuille and Werner*, 2005; *Tindall et al.*, 2009]. Model-based approaches help elucidate the relationship between ENSO and hydrologic variability, but they have not fully explored the characteristics of changes in ENSO expressions, including isotopic variability, under differing mean climate states.

In this present study, we investigate modeled hydrological expressions of ENSO-like climatic modes around the tropical Pacific using multiple simulations of past and present climates. By employing the isotope-enabled Goddard Institute for Space Studies (GISS) ModelE GCM, we investigate the pattern of isotopic anomalies associated with forced ENSO-like events under varying boundary conditions. In addition, we incorporate a novel set of vapor source distribution (VSD) tracers as an additional diagnostic tool to assess changes in atmospheric circulation at proxy sites in present-day ENSO-sensitive regions. We use modeled mid-Holocene time slices forced by ENSO-like sea surface temperature anomalies and examine whether ENSO-associated hydrological expressions in the mid-Holocene necessarily follow those simulated during the preindustrial. Overall, this study provides a model-based understanding of the potential nonstationarity of ENSO-like hydrological expressions during the mid-Holocene compared to the preindustrial.

2. Methods

2.1. Model Description

Simulations were made using the coupled atmosphere-ocean GISS (Goddard Institute for Space Studies) ModelE-R, which is the version submitted to the Coupled Model Intercomparison Project Phase 3 (CMIP3), with the addition of water isotope and tracers. The horizontal resolution is 4° latitude × 5° longitude with 20 vertical levels up to 0.1 hPa in the atmosphere [*Schmidt et al.*, 2006] and a 13 layer Russell ocean model of the same horizontal resolution [*Hansen et al.*, 2007]. Water isotope tracers (^{1}H$_2^{16}$O, "normal" water; ^{2}H^{1}H^{16}O or HDO, reported as δD; and ^{1}H$_2^{18}$O, δ^{18}O) are incorporated into the atmosphere, land surface, sea ice, and ocean. Water isotopes are tracked through all stages of the hydrologic cycle and are advected throughout the

Table 1. Summary of Model Boundary Conditions for the 0 k and 6 k Experiments Analyzed Here, Including Greenhouse Gases [*Indermuhle et al.*, 1999] and Perihelion in Julian Days [*Berger and Loutre*, 1991][a]

Time (kyr)	ENSO Phase	CO_2 (Fraction)	CH_4 (Fraction)	N_2O (Fraction)	Perihelion	Prescribed Surface Temperatures
0 k	NEUTRAL	1	1	1	2.85	N/A
	WARM	1	1	1	2.85	El Niño-like average surface temperature anomalies
	COOL	1	1	1	2.85	La Niña-like average surface temperature anomalies
6 k	NEUTRAL	0.95	0.71	0.82	263.42	N/A
	WARM	0.95	0.71	0.82	263.42	El Niño-like average surface temperature anomalies
	COOL	0.95	0.71	0.82	263.42	La Niña-like average surface temperature anomalies

[a]For each time slice, parallel experiments are also conducted with positive and negative ENSO-like surface temperature phases ($ENSO_{WARM}$ and $ENSO_{COOL}$). Sea surface temperatures for ENSO-like phases are derived from observational temperatures [*Reynolds and Smith*, 1994] and NINO3.4 indices over the period of 1981 to 2003.

model like water. At each phase change a fractionation is applied that explicitly determines equilibrium fractionation, with parameterizations accounting for kinetic fractionations [*Schmidt et al.*, 2005].

In addition to the water isotope module, we include a suite of water vapor source distribution tracers in the model so that sources of water vapor can be traced back through any cloud processes to the site of surface evaporation. The use of VSD tracers provides an additional circulation diagnostic for identifying regional-scale hydrological changes. The tracers are altered by atmospheric transport and condensation processes analogously to a nonfractionating water isotope tracer [*Kelley*, 2003]. The VSD is the integrated mass of water vapor in each model cell and is expressed as an area integral of evaporative input unique to that cell. This study uses spherical harmonics as VSD basis functions, which are not anchored to any particular geographic boundary and require no prior definition of regions. The precipitation source distribution is a subset of the VSD, defined where vapor condenses to liquid. We include 144 tracers that are resolved to wave number 11, providing an effective horizontal resolution to approximately 8° latitude × 10° longitude. It should be noted that factors such as land-sea contrasts cause real-world precipitation source distributions to vary unevenly over planetary scales, and hence, spatial VSD patterns cannot be interpreted at scales finer than their effective resolution.

2.2. Experimental Design

We conducted the experiments for this study in several stages (Table 1). As the VSD tracers are expensive to compute, an initial series of coupled atmosphere-ocean simulations were run without the VSD tracers [*LeGrande and Schmidt*, 2009]. These coupled simulations were run to equilibrium (100 s to 1000 years) for preindustrial (0 k) and mid-Holocene (6 kyr BP, "6 k") [*LeGrande and Schmidt*, 2009] mean climate conditions. The preindustrial control simulation (0 k) was run with all boundary conditions and atmospheric composition appropriate to the preindustrial period (circa 1880). In the 6 k experiment, greenhouse gas concentrations were adjusted according to ice core reconstructions [*Indermuhle et al.*, 1999; *Brook et al.*, 2000; *Sowers et al.*, 2003]; seasonal insolation was also changed relative to orbital forcings [*Berger and Loutre*, 1991].

The second phase of our experiment includes the VSD tracers, but in atmosphere-only simulations where surface conditions (SST and sea ice) are determined from the described coupled simulations. The atmosphere-only, VSD-enabled model was run for 6 years, with the average of the final 5 years' results reported here. Using this approach, once the sea surface conditions are determined (from long runs to equilibrium using the coupled model), the atmospheric model can be driven for much shorter runs using the surface conditions determined from the coupled model. A preindustrial simulation with VSD tracers included was also conducted in fully coupled mode in order to test the validity of using results from atmosphere-only simulations, and this shows only small differences in precipitation source distributions, indicating that the atmosphere-only approach is valid.

Next, we performed a set of ENSO-like simulations for each of our mid-Holocene and preindustrial experiments, in which either strong El Niño (warm) or La Niña (cool) surface temperature anomalies are imposed in the model in order to force an atmospheric response. We create a global composite of El Niño and La Niña anomalies using observational temperatures [*Reynolds and Smith*, 1994] and NINO3.4 indices over the period of 1981 to 2003. We regress NINO3.4 indices over this period with monthly mean observed surface air temperatures (SATs) to produce La Niña-like ("$ENSO_{COOL}$") and El Niño-like ("$ENSO_{WARM}$") conditions that are
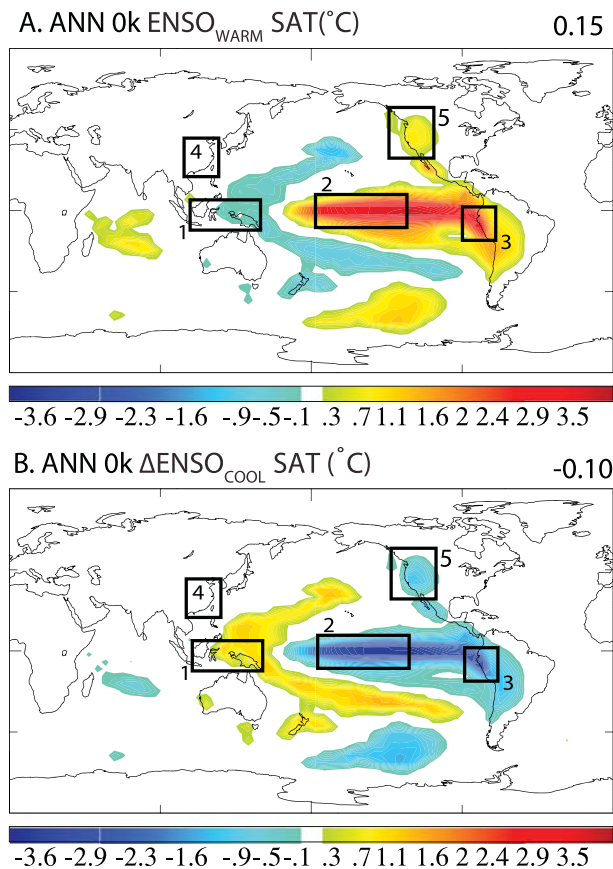
Figure 1. Annual average surface air temperature anomalies (°C) used as boundary conditions for the (a) ENSO$_{WARM}$ and (b) ENSO$_{COOL}$ simulations, relative to the preindustrial control mean. Average observed surface temperature anomalies [*Reynolds and Smith*, 1994] associated with strong (×3) El Niño- (ENSO$_{WARM}$) and La Niña-like (ENSO$_{COOL}$) conditions are determined from the NINO3.4 index and applied to SAT fields for the 0 k simulations as surface boundary conditions. Also shown are the locations of five defined regions of interest: the western (1), eastern (2) and central Pacific (3), eastern China (4), and northwest (NW) Pacific (5). Figure adapted from *Lewis et al.* [2013].

applied as surface boundary conditions for the preindustrial simulations. This technique produces surface temperature conditions that are broadly representative of positive and negative ENSO phases, although the regression was multiplied by a factor of 3 to ensure that the fingerprint of this type of climatic change is discernible throughout the hydrological cycle [*Hoerling et al.*, 2001; *Chung et al.*, 2014]. To put the temperature anomalies used into context, the corresponding NINO3.4 anomaly applied in our study is approximately equal to that occurring during the strong El Niño event during 1997–1998. Overall, we produce a preindustrial experiment suite with three ensemble members (0 k ENSO$_{WARM}$, 0 k ENSO$_{COOL}$, and 0 k ENSO$_{NEUTRAL}$) that represent average, perpetual El Niño-, La Niña-, and neutral-like conditions. The surface temperature anomalies used for ENSO$_{WARM}$ and ENSO$_{COOL}$ are shown in Figure 1.

In addition, ENSO-like surface anomalies were also applied to the mid-Holocene for the various phases ("6 k ENSO$_{WARM}$" and "6 k ENSO$_{COOL}$") to investigate whether the fingerprint of ENSO-like variability on the hydrological cycle is sensitive to differing boundary conditions. For this experiment set, ENSO-like anomalies were applied as surface boundary conditions to mid-Holocene surface temperature and sea ice anomalies, which were calculated as differences between mean mid-Holocene and preindustrial conditions so that forced ENSO and forced mid-Holocene response could be separated. This results in a second experiment suite with three ensemble members—6 k ENSO$_{WARM}$, 6 k ENSO$_{COOL}$, and 6 k ENSO$_{NEUTRAL}$. Although the amplitude and precise spatial pattern of ENSO activity in the mid-Holocene remains uncertain, we apply the same strong surface temperature forcing to both time slices to allow comparison of ENSO-like impacts on the tropical hydrological cycle under these different boundary conditions. These results are not presented for direct comparison with proxy records but rather as idealized experiments that help elucidate changing ENSO
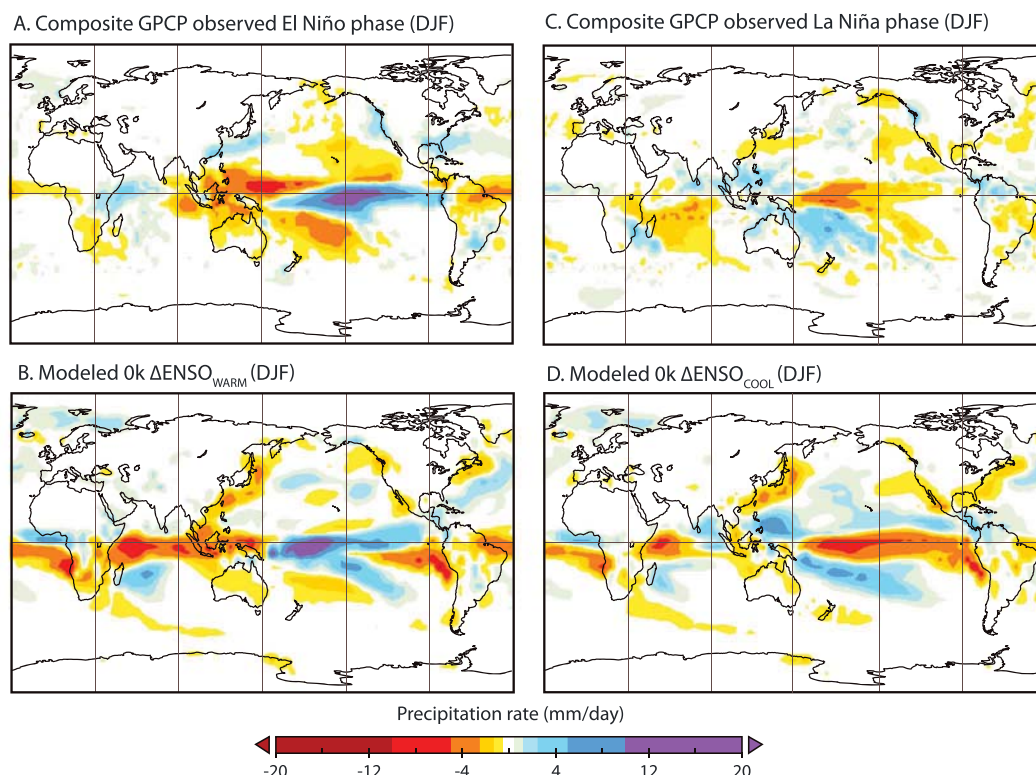
A. Composite GPCP observed El Niño phase (DJF)

C. Composite GPCP observed La Niña phase (DJF)

B. Modeled 0k ΔENSO$_{WARM}$ (DJF)

D. Modeled 0k ΔENSO$_{COOL}$ (DJF)

Precipitation rate (mm/day)

-20   -12   -4   4   12   20

Figure 2. Comparison of average December–February composite GPCP observational (a) El Niño precipitation anomalies with (b) simulated precipitation ΔENSO$_{WARM}$ anomalies (mm/d, relative to preindustrial simulation) and comparison of average December–February composite GPCP observational (c) La Niña precipitation anomalies with (d) simulated precipitation ENSO$_{COOL}$ anomalies (mm/d, relative to preindustrial simulation). Observational El Niño (La Niña) precipitation anomalies (relative to a 1981–2005 climatology) are composites of 1982 and 1997 (1988 and 1999) (wherein sea surface temperature anomalies in the NINO3.4 region exceeded 2 standard deviations above (below) average for six consecutive months and represent strong El Niño (La Niña) events).

teleconnection patterns and moisture source changes under varying boundary conditions. This approach also avoids relying on the model's ability to realistically capture intrinsic, freely evolving ENSO activity, which is inherently limited by model resolution and parameterizations, as well as our theoretical understanding of ENSO dynamics [*Meehl et al.*, 2001]. The ENSO-like results should be interpreted in general terms, given the forcing applied corresponds to strong ENSO activity in a contemporary context.

3. Evaluation of Model Performance

In previous studies, isotope and precipitation distributions simulated with GISS ModelE-R have been systematically compared to observational records for the preindustrial [*Schmidt et al.*, 2006, 2007] and evaluated against proxy records for the mid-Holocene [*LeGrande and Schmidt*, 2009]. Patterns of ModelE-R simulated $\delta^{18}O_p$ are highly correlated with observed fields, although rainfall in the western Warm Pool region is in excess of observed GPCP (Global Precipitation Climatology Project) patterns [*Schmidt et al.*, 2006]. Similarly, simulated mean Holocene East Asian $\delta^{18}O_p$ and surface ocean $\delta^{18}O$ values correspond closely with those reported in regional proxy records, and the large-scale features of climatic change in the mid-Holocene are captured by the model [*LeGrande and Schmidt*, 2009].

In addition to the previous evaluation of the hydrological responses in these preindustrial and mid-Holocene model experiments, we evaluate the utility of the ENSO-like experiments for assessing changes in hydrological responses by comparing simulated spatial patterns with observed precipitation distributions (Figure 2). Simulated ENSO$_{WARM}$ and ENSO$_{COOL}$ precipitation fields are compared to the GPCP gridded data sets [*Adler et al.*, 2003], where the observed anomalies associated with strong El Niño conditions (i.e., in 1982 and 1997) and strong La Niña conditions (i.e., in 1988 and 1999) were composited. The similarity of

Table 2. Summary of December–February Regional Areal-Average Precipitation (mm/d), $\delta^{18}O_p$ (‰), and SAT (°C) Anomalies Associated With Neutral, $\Delta ENSO_{WARM}$, and $\Delta ENSO_{COOL}$ Conditions for Observations and 0 k (Preindustrial Control) and 6 k (Mid-Holocene) Model Experiments[a]

		Observed			Modeled 0 k			Modeled 6 k		
		$ENSO_{NEUTRAL}$	$\Delta ENSO_{WARM}$	$\Delta ENSO_{COOL}$	$ENSO_{NEUTRAL}$	$\Delta ENSO_{WARM}$	$\Delta ENSO_{COOL}$	$ENSO_{NEUTRAL}$	$\Delta ENSO_{WARM}$	$\Delta ENSO_{COOL}$
Western Pacific	PR	7.0	−2.6	0.6	6.6	−2.1	0.6	8.9	−1.2	1.1
	$\delta^{18}O_p$				−4.1	1.9	−0.3	−6.0	1.4	−0.4
	SAT	27.1	0.4	0.3	26.8	0.0	0.2	26.3	0.0	0.3
Central Pacific	PR	3.6	5.5	−0.8	9.0	4.9	−1.4	3.9	3.7	−1.5
	$\delta^{18}O_p$				−5.1	−2.3	0.3	−2.7	−1.8	0.4
	SAT	25.5	0.3	−0.9	27.8	1.7	−2.1	25.5	1.8	−2.0
Eastern Pacific	PR	4.0	0.5	0.1	4.1	−0.3	0.0	4.1	−0.3	0.0
	$\delta^{18}O_p$				−5.6	1.9	0.3	−7.4	1.9	0.7
	SAT	24.9	2.9	−1.9	25.1	1.6	−0.7	22.8	1.5	−0.4
Eastern China	PR	1.4	0.5	−0.1	2.6	−0.2	0.2	2.5	−0.1	0.4
	$\delta^{18}O_p$				−7.8	0.1	−0.2	−8.5	0.0	−0.2
	SAT	14.0	−1.3	−1.5	10.7	0.1	−0.4	9.3	0.1	−0.5
NW Pacific	PR	3.3	0.7	−0.2	2.9	0.3	−2.7	2.7	0.3	0.0
	$\delta^{18}O_p$				−11.6	0.7	−0.2	−12.8	0.5	−0.1
	SAT	5.5	−0.3	−1.0	2.4	1.3	−0.3	0	1.7	2.6

[a]Observed precipitation anomalies from GPCP data set [Adler et al., 2003] and SAT anomalies from HadCRUT4 data set [Morice et al., 2012]. Observed 0 k values are averages over the entire period available, and observed $\Delta ENSO_{WARM}$ ($\Delta ENSO_{COOL}$) anomalies are composites of 1982 and 1997 (1988 and 1999) (wherein sea surface temperature anomalies in the NINO3.4 region exceeded 2 standard deviations above (below) average for six consecutive months and represent strong El Niño (La Niña) events).

observed (strong El Niño) and simulated ($ENSO_{WARM}$) composite responses is seasonally variable; spatial anomalies are most similar in December–February (Figure 2) compared to during June–August (not shown). Similarly, observed and simulated $ENSO_{COOL}$ phase anomalies are most alike in the boreal summer, although the simulated dry conditions over the central Pacific are notably zonal compared with observed. While the simulated precipitation responses in the ENSO-like experiment is generally stronger than those observed during these noteworthy ENSO events, we consider these experiments to be insightful for examining potential changes in responses under varying boundary conditions. However, as ENSO events typically reach their peak amplitude in the boreal winter (December–February (DJF)) [McGregor et al., 2013b], we consider modeled changes during this season only.

In this study, model data are investigated in five regions (Figure 1, western, eastern and central Pacific, eastern China, and northwest (NW) Pacific) that are identified as sensitive to contemporary ENSO variability, providing coverage of simulated hydrological change across the Pacific basin and encompassing the location of numerous proxy archives utilized in paleoclimate reconstructions of the Holocene. These regions are not intended to provide exhaustive coverage of ENSO impacts, and hence, regions exhibiting significant ENSO-related climatological anomalies that do not encompass proxy archives, such as in the South Pacific and Indian Oceans, are not discussed explicitly.

Simulated precipitation anomalies in these regions for $ENSO_{WARM}$ and $ENSO_{COOL}$ conditions are compared with observations in Table 2, showing that observed precipitation amount anomalies associated with strong observed El Niño and La Niña events are generally well captured in the model simulations in these regions.
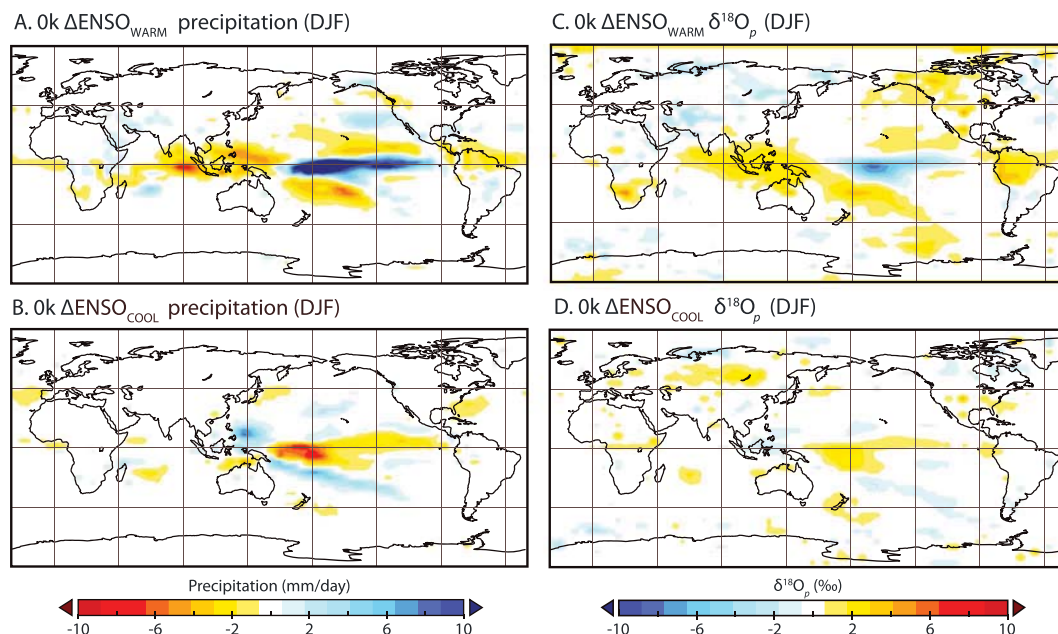
Figure 3. Large-scale simulated (a, b) DJF precipitation (mm/d) and (c, d) $\delta^{18}O_p$ (‰) anomalies for the preindustrial simulation, showing ENSO$_{WARM}$ and ENSO$_{COOL}$ changes relative to neutral conditions. All values reported are greater than 95% significant (Student's t test) given the year-to-year variability about the 5 year mean.

Most notably, the simulated precipitation amount (3.6 mm/d) in the central Pacific is subdued relative to observed (9 mm/d), although only anomalies are considered in this study to account for consistent biases. Observed surface air temperatures and anomalies for ENSO$_{WARM}$ and ENSO$_{COOL}$ conditions are also generally well captured in the model simulations. Simulated temperature anomalies are most disparate for the positive El Niño-like phase for the NW Pacific and eastern China regions, although it should be noted that these are compared to a limited number of observed years when other climate drivers may have also been regionally important. A detailed evaluation of simulated isotopic responses in these experiments is provided in the supporting information.

4. Results

The ENSO anomalies presented here represent the difference between the ENSO$_{WARM}$ or ENSO$_{COOL}$ experiment and the ENSO neutral (ENSO$_{NEUTRAL}$) experiments. For example, using this notation, differences between simulated El Niño-like (La Niña-like) and neutral conditions in the preindustrial (0 k) experiment would be indicated as 0 k ΔENSO$_{WARM}$ (0 k ΔENSO$_{COOL}$). Similarly, we denote mid-Holocene anomalies relative to preindustrial (0 k) values by Δ6k. Unless otherwise indicated, mid-Holocene changes refer to mean ENSO$_{NEUTRAL}$ anomalies. Values reported here are greater than 95% significant (Student's t test), given year-to-year variability.

4.1. ENSO-Like Hydrological Changes

Simulated $\delta^{18}O_p$ and precipitation ENSO anomalies (ΔENSO$_{WARM}$ and ΔENSO$_{COOL}$) for the preindustrial experiment set are shown in Figure 3 and summarized in Table 2. Under the warm sea surface temperature conditions in the tropical Pacific (characterizing the ENSO$_{WARM}$ experiment), there is an increase in precipitation in the equatorial Pacific and decreases in the western Pacific around the Warm Pool. Simulated isotopic differences are spatially more variable than differences in precipitation amount between the ENSO$_{WARM}$ and neutral experiments: ENSO-associated $\delta^{18}O_p$ anomalies extend to the high latitudes and display less spatial coherence than rainfall changes. Spatially variable $\delta^{18}O_p$ model responses, compared with precipitation changes, have been previously noted for other model experiments [*Schmidt et al.*, 2005; *Lewis et al.*, 2010]. Generally, ENSO$_{WARM}$ $\delta^{18}O_p$ is enriched (compared with neutral conditions) over the Warm

A. Western Pacific 0k ENSO$_{NEUTRAL}$ VSD (DJF)

B. Central Pacific 0k ENSO$_{NEUTRAL}$ VSD (DJF)

C. Eastern Pacific 0k ENSO$_{NEUTRAL}$ VSD (DJF)

D. Eastern China 0k ENSO$_{NEUTRAL}$ VSD (DJF)

E. NW Pacific 0k ENSO$_{NEUTRAL}$ VSD (DJF)

precipitation source
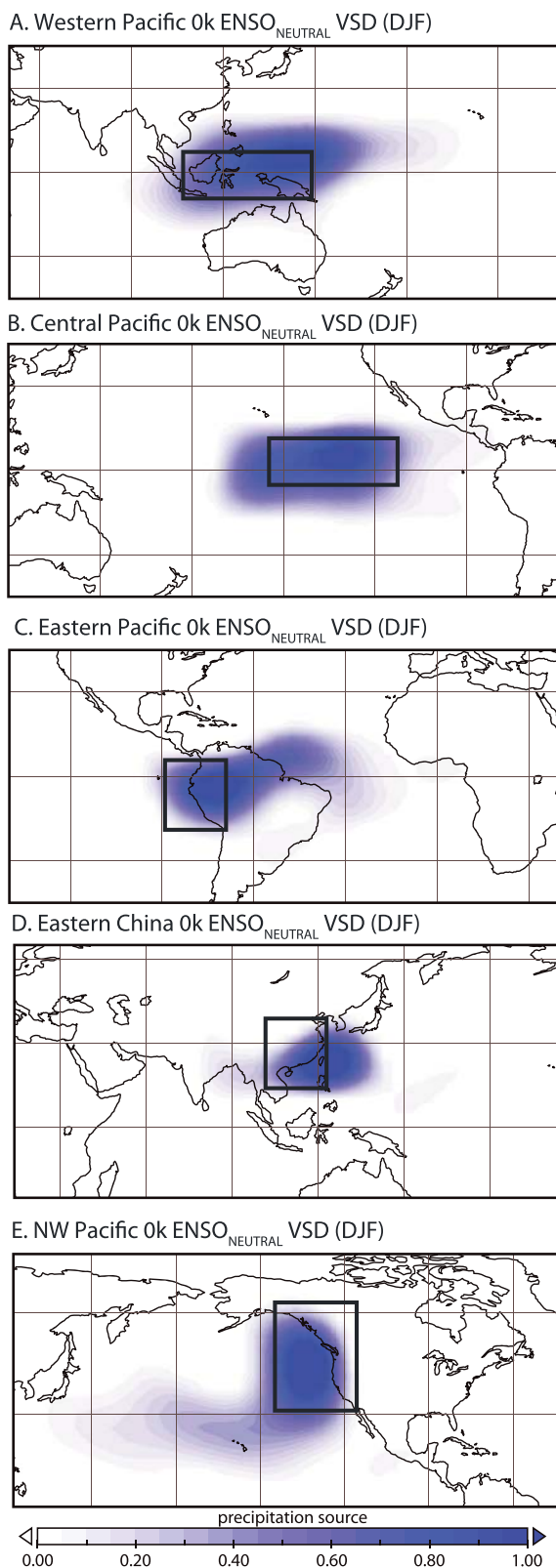
0.00   0.20   0.40   0.60   0.80   1.00

Figure 4. Simulated vapor source distributions (VSDs) for each analyzed region ((a) western Pacific, (b) central Pacific, (c) eastern Pacific, (d) eastern China, and (e) NW Pacific), showing the source for each region in the preindustrial simulation for the ENSO neutral phase. The solid rectangular boxes indicate the location of end-member precipitation. VSDs are unitless probability density function, normalized by the maximum probability density.

Pool region, extending through to the northern Indian Ocean. Conversely, over the eastern and central equatorial Pacific, there is a $\delta^{18}O_p$ depletion during the ENSO$_{WARM}$ phase.

There are areas over Australia, Africa, tropical South America, and the western USA in which distinct $\delta^{18}O_p$ responses to the ENSO$_{WARM}$ and ENSO$_{COOL}$ forcings are simulated, although no comparable differences in rainfall amount occur. Certain areas may be recording complex changes in hydrology, such as moisture source region, beyond simple deviations in rainfall amount alone [*Vuille and Werner*, 2005; *Schmidt et al.*, 2007; *LeGrande and Schmidt*, 2009]. Changes in moisture source regions to particular sites provide both an important control on $\delta^{18}O_p$ composition [*Rozanski et al.*, 1993] and a useful circulation diagnostic for considering regional-scale hydrological change [*Lewis et al.*, 2010].

Regionally specific moisture source tracers demonstrate source changes during ENSO-like phases, relative to neutral conditions (Figures 4 and 5), and differences in regional hydrology occur across the Pacific basin between El Niño-like and La Niña-like events. Source region shifts associated with ENSO$_{WARM}$ conditions are generally stronger than the ENSO$_{COOL}$, while the spatial patterns of change are distinct (Figure 5). That is, the ENSO$_{WARM}$ anomalies, relative to neutral, do not necessarily mirror those associated with the ENSO$_{COOL}$ phase in all regions. An asymmetry in the ENSO-tropical rainfall teleconnection has been noted previously in response to a zonally symmetric ENSO forcing [*Power et al.*, 2006; *Chou and Lo*, 2007]. The source region shifts associated with the ENSO$_{COOL}$ experiment are largest in the central Pacific. The impact on the hydrological cycle of these ENSO-like surface temperature changes, even beyond the tropics, is also notable in the eastern China and northwest Pacific regions, although it should be reiterated that strong surface temperature anomalies were applied to these experiments as a forcing. In addition, the ENSO-phase source region changes are largely distinct from other climate modes, such as the seasonal cycle (not shown), although the amplitude of the moisture source response is comparable.

4.2. Mid-Holocene Hydrological Changes

In the mid-Holocene, simulated global DJF surface temperatures are 0.5°C cooler than the preindustrial (Annual (ANN), 0.35°C and June–August (JJA), 0.2 C). Climatological changes in the mid-Holocene, compared with the preindustrial, largely relate to insolation anomalies. In particular, due to changes in precession, there was reduced mid-Holocene insolation during DJF, resulting in cooler boreal winters and austral summers. In DJF, the spatial pattern of mean simulated temperature changes is characterized by cooling in the tropics, midlatitudes of the Northern Hemisphere, and southern high latitudes (Figure 6). Conversely, there is warming in the mid-Holocene in the high northern latitudes, compared with the preindustrial, due to increased wintertime insolation and the resulting, persistent reduction in sea ice [*LeGrande and Schmidt*, 2009].

Simulated mid-Holocene hydrological anomalies are less spatially coherent than surface air temperature changes. Precipitation amount anomalies are centered on the tropics, with mid-Holocene rainfall decreases simulated over the equatorial Pacific, southern Africa, South America, and Australia. Increases in precipitation are simulated across the Indian Ocean and Warm Pool region. The globally averaged mid-Holocene precipitation amount anomaly is 0.01 mm/d for DJF (ANN, -0.2 mm/d and JJA, -0.05 mm/d). The rainfall anomalies in the mid-Holocene, associated with orbital changes, are substantially smaller than those associated with the imposed ENSO-like forcings for the preindustrial (Figure 2), which are up to an order of magnitude higher. The simulated $\Delta 6k$ $\delta^{18}O_p$ anomalies during DJF are more spatially widespread than the rainfall and surface air temperature changes, relative to the preindustrial. There are simulated isotopic enrichments throughout the high northern latitudes during the boreal winter and large-scale isotopic depletions across Eurasia and the Indian Ocean. The isotopic responses to insolation forcing in the mid-Holocene are similarly muted in comparison to the magnitude of the $\delta^{18}O_p$ anomalies during DJF associated with ENSO-like conditions (Figure 2).

4.3. Mid-Holocene ENSO-Like Teleconnection Changes

Comparison of $\delta^{18}O_p$ and precipitation anomalies between the preindustrial and mid-Holocene indicates that the spatial patterns of change associated with ENSO-like phases are similar in each experiment (Figures 3 and 7), with spatial fields highly correlated between the mid-Holocene and preindustrial ($R > 0.95$). The ENSO-like precipitation amount and $\delta^{18}O_p$ changes are somewhat subdued in the mid-Holocene, in terms of both the magnitude of hydrological changes and their spatial extent. However, the precipitation source
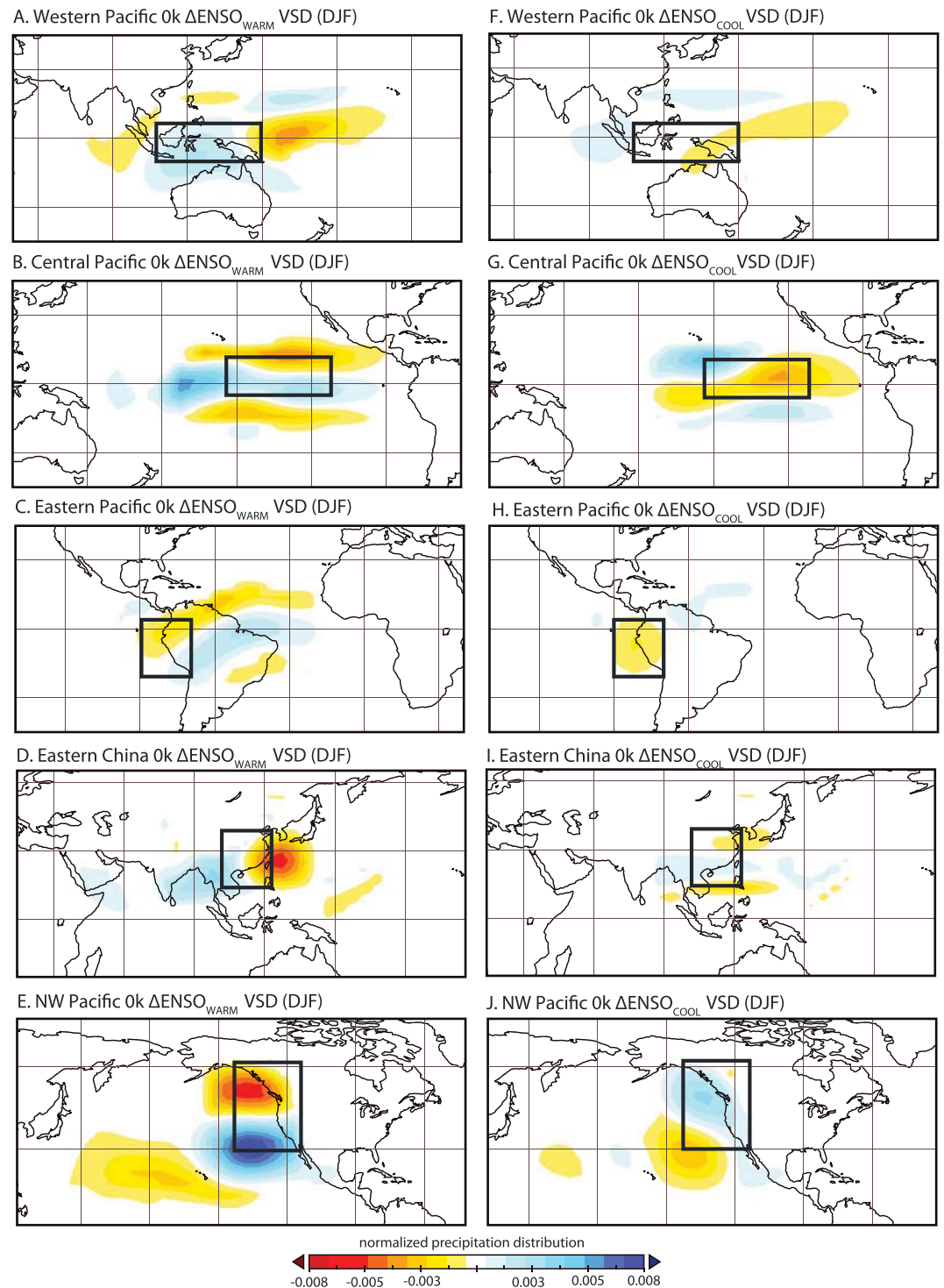
Figure 5. Simulated vapor source distributions (VSDs) for each analyzed region ((a, f) western Pacific, (b, g) central Pacific, (c, h) eastern Pacific, (d, i) eastern China, and (e, j) NW Pacific), showing the difference (ΔENSO) between the ENSO$_{WARM}$ and neutral phases in the preindustrial control experiment (Figures 5a–5e). The ΔENSO$_{COOL}$ differences in the preindustrial simulations, relative to neutral, are also shown (Figures 5f–5j). The solid rectangular boxes indicate the location of end-member precipitation. VSDs are unitless probability density function, normalized by the maximum probability density.
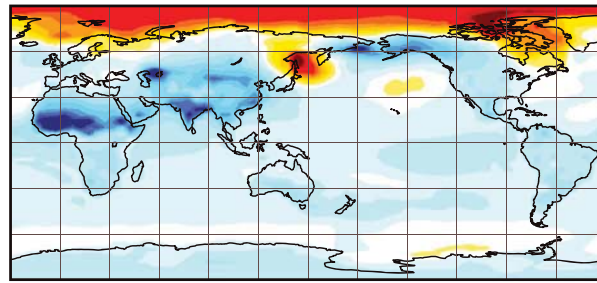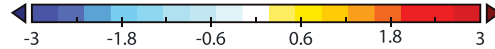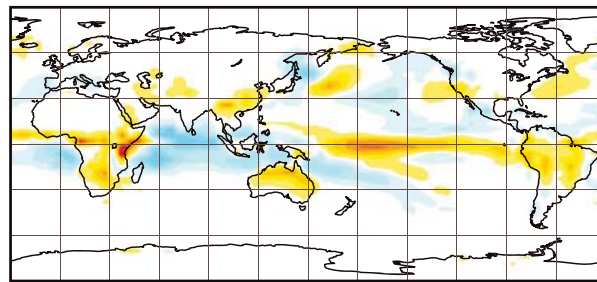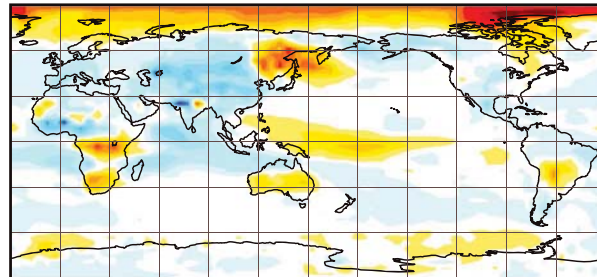
Figure 6. DJF seasonal average SAT (°C), precipitation (mm/d), and $\delta^{18}O_p$ (‰) anomalies (Δ6 k) for the mid-Holocene, relative to the preindustrial simulation. All values reported are greater than 95% significant (Student's *t* test) given the year-to-year variability about the 5 year mean. Figure adapted from *LeGrande and Schmidt* [2009].

distributions for each of the analyzed regions (Figure 8) reveal a more complex relationship between ENSO-like expressions and the boundary conditions associated with the preindustrial and mid-Holocene experiments. That is, source region difference between the mid-Holocene and the preindustrial are less notable for the neutral ENSO conditions than when ENSO-like forcings are applied. The comparatively more pronounced impacts of ENSO_COOL and ENSO_WARM, than neutral, conditions are a basin-wide phenomenon, impacting all regions analyzed here.

For the western Pacific region, for example, there is a more westward (and localized) moisture source to the region of interest during the mid-Holocene ENSO_WARM experiment than with equivalent surface temperature forcings applied during the preindustrial. Similarly, more localized moisture sources to the western Pacific region are simulated mid-Holocene ENSO_WARM experiment, with a decrease in rainfall sources from the equatorial Pacific, compared with the Warm Pool region. In addition, the spatial
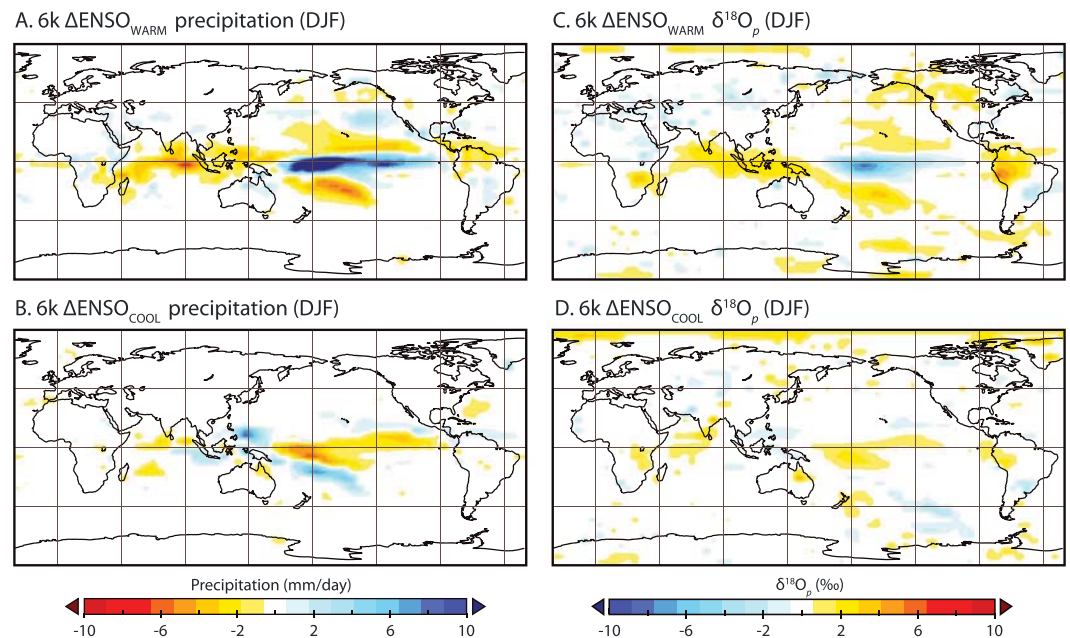
Figure 7. As for Figure 3 but showing mid-Holocene precipitation (mm/d) anomalies and $\delta^{18}O_p$ (‰) anomalies for (a, c) ENSO$_{WARM}$ and (b, d) ENSO$_{COOL}$ changes, relative to neutral conditions.

patterns of $\Delta 6k$ anomalies for the ENSO$_{COOL}$ experiment do not necessarily mirror those for the ENSO$_{WARM}$ experiment. For example, the differences between the mid-Holocene and preindustrial source distributions for the northwestern Pacific are weaker for the La Niña-like experiment suite than for the El Niño-like experiments.

Comparing simulated surface wind changes between the mid-Holocene and preindustrial for the ENSO$_{WARM}$ and ENSO$_{COOL}$ phases also reveals subtle but potentially important differences (Figure 9). Changes during the mid-Holocene include an outflow of surface air from eastern Asia, compared to the preindustrial, which shows landward airflow. The character of surface winds in the ENSO-like experiments is also notably different in the mid-Holocene compared to the preindustrial. For the ENSO$_{WARM}$ phases, particularly in the northern Pacific, flow is more zonally oriented during the preindustrial, and convergence along the equatorial Pacific is strong. Also, for the ENSO$_{COOL}$ phase, the character of surface wind flow in the northwestern Pacific is distinct between the preindustrial and mid-Holocene, where convergence in the northern Pacific is weaker and shifted southwestward, which likely relates to modeled source region shifts (Figures 5 and 8). Hence, although the relationship between $\delta^{18}O_p$ and precipitation may be relatively stable for some areas under differing boundary conditions, the vapor source tracers and surface wind fields suggest that the interaction between ENSO-like variability and the large-scale ocean-atmosphere states (i.e., boundary conditions) may elicit nonlinear hydrological responses that warrant further investigation.

5. Discussion

5.1. Stability of Mid-Holocene ENSO-Like Expressions

The assumption of stationarity in climatic relationships between regions underpins many paleoclimatic reconstructions. However, teleconnected climatic relationships are influenced by changes in the large-scale state of the coupled ocean-atmosphere systems that may have implications for paleoclimate research aiming to reconstruct changes in ENSO variability from information gleaned from one site alone [*Gallant et al.*, 2013]. As a simplistic assessment of potential differences in ENSO-like expressions between the preindustrial and mid-Holocene, we compared the relationship between $\delta^{18}O_p$ and precipitation amount across the different experiments (Figure 10). In certain regions, there is a clear distinction in the relationship between $\delta^{18}O_p$ and rainfall amount between the mid-Holocene and preindustrial for the various ENSO-like phases. For example, for
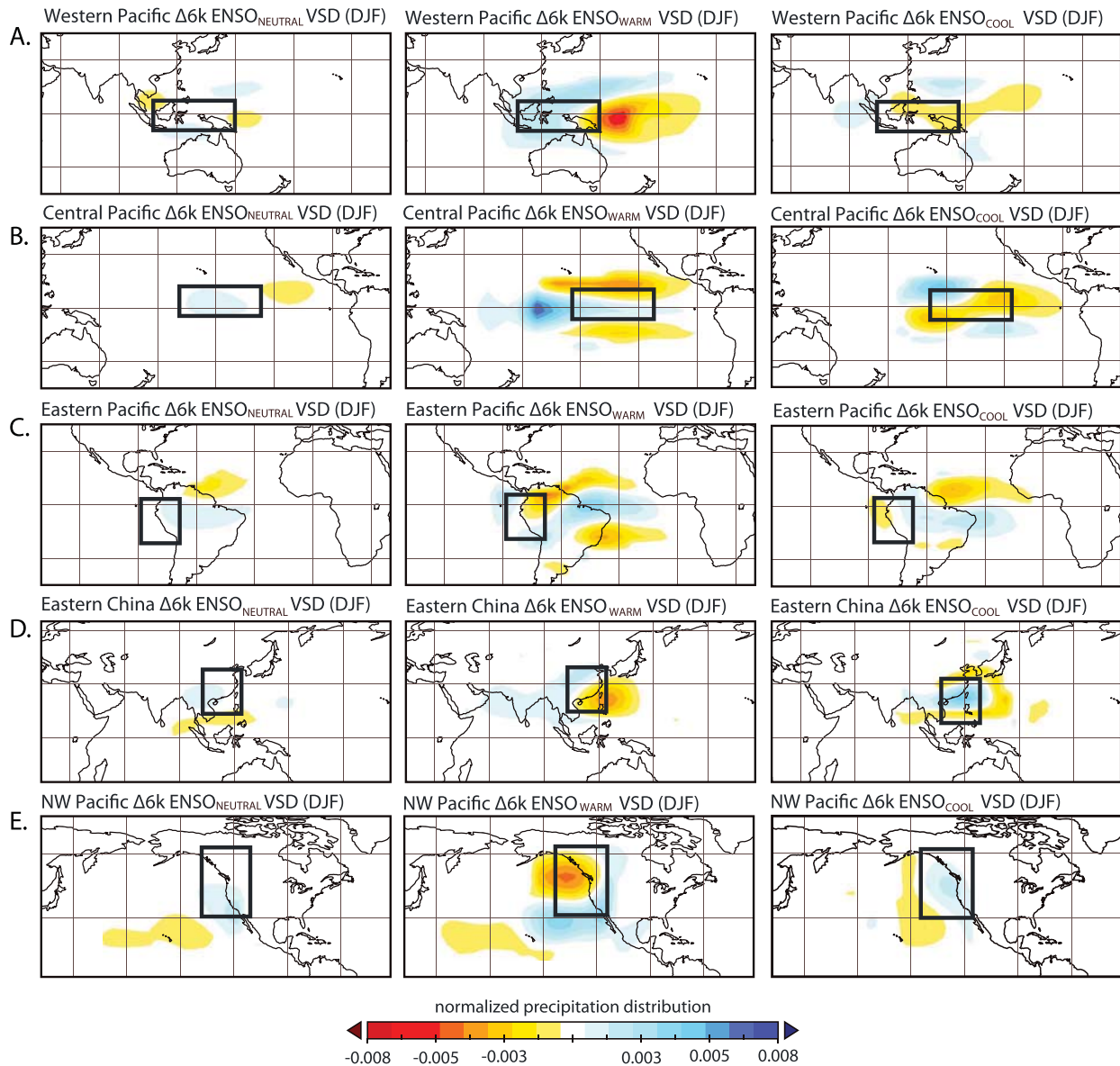
Figure 8. Simulated December–February precipitation source distributions for each region ((a) western Pacific, (b) central Pacific, (c) eastern Pacific, (d) eastern China, and (e) NW Pacific), showing the difference (Δ6 k) between the preindustrial control (0 kyr) and the mid-Holocene (6 kyr) for each ENSO-like phase ((left) $ENSO_{NEUTRAL}$, (middle) $ENSO_{WARM}$, and (right) $ENSO_{COOL}$). The solid rectangular boxes indicate the location of end-member precipitation. VSDs are unitless probability density function, normalized by the maximum probability density.

the northwestern Pacific region, the $\delta^{18}O_p$-precipitation anomalies for $ENSO_{WARM}$ conditions (relative to neutral) are similar in both the preindustrial and the mid-Holocene (Figure 10e), although the $ENSO_{COOL}$ hydrological impact in this region is far more pronounced in the preindustrial and may relate to source region changes. Similarly, for the western and central Pacific region, the mid-Holocene, and preindustrial $\Delta ENSO_{COOL}$ anomalies are comparable, while the $ENSO_{WARM}$ phase anomalies are comparatively larger in the preindustrial than for 6 kyr. Next, for the eastern China region, the difference in the $\delta^{18}O_p$-precipitaiton relationship between the mid-Holocene and preindustrial is comparable for the $ENSO_{WARM}$ and $ENSO_{COOL}$ phases (Figure 10d).

Although this a simple metric of ENSO-like changes, it is clear that La Niña-like and El Niño-like hydrological expressions during the mid-Holocene will not necessarily follow those occurring during the preindustrial. In particular, the mid-Holocene hydrological ($\delta^{18}O_p$ and precipitation amount) responses to $ENSO_{WARM}$ and $ENSO_{COOL}$ phases are largely muted compared to the preindustrial, even though the same surface
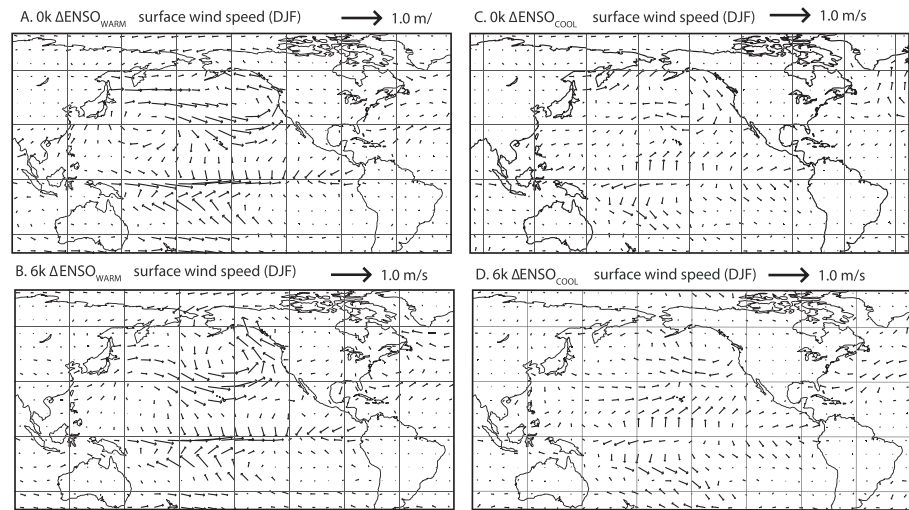
Figure 9. Seasonal (DJF) surface wind speed anomalies (m/s) for the Pacific region for ΔENSO$_{WARM}$ and ΔENSO$_{COOL}$ for the (a, c) preindustrial and (b, d) mid-Holocene. Vectors indicate the direction of wind speed anomalies.

temperature forcings are imposed for both time slices. While the simulated $\delta^{18}O_p$ and precipitation amount responses to ENSO-like forcings are subdued in the mid-Holocene, changes are simulated in other circulation diagnostics, such as the moisture source regions to the analyzed regions. When comparing source region changes during ENSO-like conditions during the preindustrial with those during the mid-Holocene (Figures 5 and 8), it is evident that ENSO-like hydrological expressions during the mid-Holocene are unique to that period.

Furthermore, there are distinct patterns of hydrological changes associated with El Niño-like and La Niña-like conditions, and the application of ENSO$_{COOL}$ forcings does not produce climatological anomalies that represent impacts of equal magnitude but opposite sign of the ENSO$_{WARM}$ experiment. Rather, as previous research has also shown, the differing phases of ENSO are capable of producing nonlinear responses in

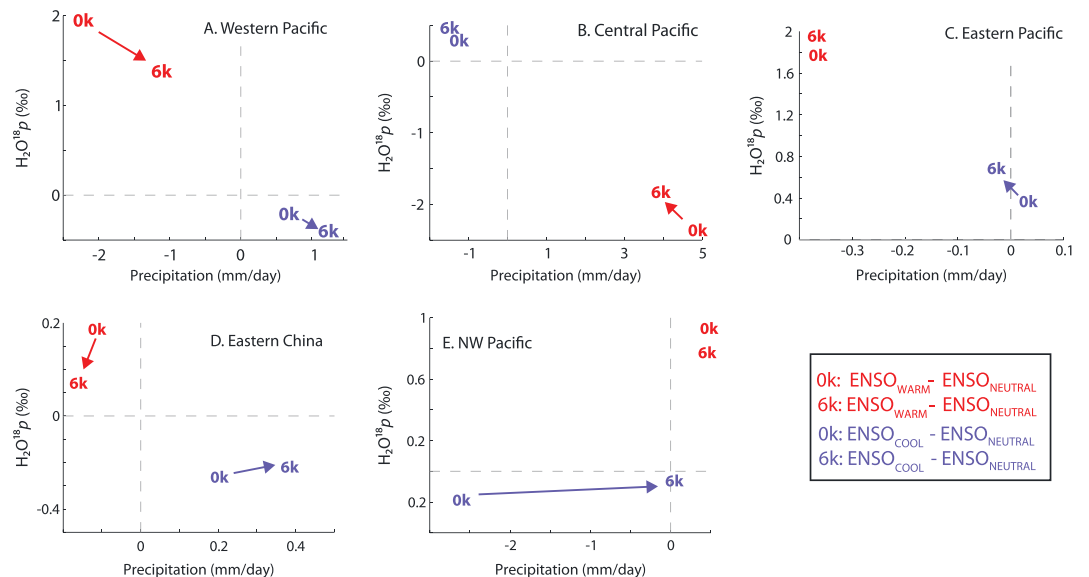**Figure 10.** Comparison of $\delta^{18}O_p$ (‰) and precipitation amount (mm/d) ENSO-like phase anomalies for the preindustrial (0 k) and mid-Holocene (6 k) experiments for each defined region ((a) western Pacific, (b) central Pacific, (c) eastern Pacific, (d) eastern China, and (e) NW Pacific). The differing ENSO-like phases, relative to ENSO$_{NEUTRAL}$, are designated by color (ΔENSO$_{WARM}$ as red and ΔENSO$_{COOL}$ as blue). Data points represent the areal average value in each of the regions, and arrows indicate the direction of statistically significant changes between the preindustrial and mid-Holocene for each phase.

precipitation, sea level pressure, and winds [*Power et al.*, 2006; *Conroy et al.*, 2013]. There are also distinct patterns of hydrological changes associated with the positive and negative ENSO phases between the preindustrial and mid-Holocene. Even in remotely teleconnected regions, there are changes associated with the ENSO-like phases that indicate nonlinear interactions between ENSO and the background state of the ocean-atmosphere system (i.e., the model boundary conditions).

Why are expressions of ENSO-like variability distinct under different model boundary conditions, such as for the mid-Holocene? First, the complexity in responses to the imposed $ENSO_{WARM}$ and $ENSO_{COOL}$ phases may relate partly to the differing mean climatic state that characterizes the mid-Holocene. The mid-Holocene tropical Pacific is generally more ENSO-like with larger temperature anomalies (relative to the preindustrial) occurring in the eastern Pacific rather than the western Pacific, despite a zonally symmetric insolation forcing (Figure 6). Hence, when surface temperature forcings are applied in distinct spatial regions (the central and eastern Pacific, compared to the western part of the basin), recognizably different responses may occur. Similarly, an increase in El Niño frequency has been simulated under projected future warming due to increased warming of the eastern equatorial Pacific, compared with the surrounding ocean [*Power et al.*, 2013; *Cai et al.*, 2014]. Modern ENSO behavior is also sensitive to changes in wind stress that relate to surface temperature anomalies [*Wittenberg*, 2004], and changes in wind stress simulated here (Figure 9) may impact the hydrological cycle through convergence and ultimately convection.

In addition, one of the predominant characteristics of ENSO is its connection to the seasonal cycle, with most recorded events reaching their maximum intensity in November–January. The phase-locking of ENSO variability to the annual cycle relates to the seasonal movement of the Intertropical Convergence Zone or zonal sea surface temperatures gradients, among other mechanisms [*Ham et al.*, 2013]. Although the differences in boundary conditions between the mid-Holocene and the preindustrial are relatively small compared to other time slices, such as the Last Glacial Maximum, there are important perturbations in radiative forcings associated with this period [*Schmidt et al.*, 2004]. The largest changes are associated with varying insolation from the mid-Holocene to the present, primarily due to changes in precession, which results in a redistribution of seasonal insolation in the tropics. Specifically, tropical areas received more (less) irradiance during the second (first) half of the year and mid-Holocene Northern Hemisphere summers had substantially more incoming solar radiation than present (>25 W/m^2 over the season). The redistribution of seasonal insolation may impact tropical ocean-atmosphere dynamics in several ways, including through the perturbation of the zonal SST gradient and easterly trade winds [*Clement et al.*, 1999]. Also, changes in meridional SST gradients across the tropical Pacific, due to differential heating, may have impacted mid-Holocene upwelling and ENSO development [*McGregor et al.*, 2013a].

5.2. Reconstructing Mid-Holocene ENSO Expressions

The impact of the mid-Holocene orbital changes on the tropical Pacific and paleo-ENSO variability has not been established comprehensively from proxy records. Proxy ENSO-sensitive records indicate various possible changes in mid-Holocene ENSO characteristics in terms of the amplitude, variability, and spatial teleconnection patterns [*Donders et al.*, 2008]. Furthermore, some records suggest a relative cooling of eastern equatorial Pacific SST [*Koutavas et al.*, 2002], while others show relative warming [*Lea et al.*, 2006]. In the western Pacific, δ^{18}O records suggest similar or slightly cooler than modern SST, whereas concomitant Sr/Ca ratios indicate slightly warm SSTs [*Tudhope et al.*, 2001]. Some fossil coral reconstructions indicate that there may have been reductions in ENSO variability in the mid-Holocene [*Cobb et al.*, 2013], with integrated multiproxy reconstructions suggesting that recognizably "modern" El Niño activity beginning roughly 5 kyr [*Donders et al.*, 2008].

Beyond the general constraints of reconstructing past climatic change from proxy archives that are often short or spatially limited, understanding paleo-ENSO variability is also complicated by the complex hydrological expressions of this large-scale phenomenon. Overall, these highly idealized experiments reveal inherent hydrological complexity associated with ENSO-like teleconnections that may impact interpretations of proxy ENSO-focused reconstructions. Our present model results, together with previous studies [*Gallant et al.*, 2013], highlight the importance of considering the potential nonstationarity of ENSO teleconnections when interpreting paleoclimate archives, especially those that rely exclusively on ENSO-related changes in precipitation. ENSO-like periodic patterns evident at proxy sites influenced by teleconnections may not necessarily reflect changes in ENSO-based frequencies but rather subtle changes in teleconnected climatological patterns

[*Shulmeister et al.*, 2006]. In this case, interpretations of interannual-scale variability in climate proxies in terms of basin-wide ENSO expressions from one or two sites alone will be necessarily problematic.

In addition, ENSO-like conditions impact many aspects of the climate system, including surface temperatures, wind speeds, and convective activity, as shown by the ENSO-forced circulation changes diagnosed by the modeled VSD tracers (Figure 8). In many regions, $\delta^{18}O_p$ variability integrates multiple climatic influences, such as changes in rainfall amount, temperature, and source regions, and hence, convoluted changes in ENSO-like expressions in the hydrological cycle are likely to make $\delta^{18}O$-climate interpretations inherently complex. For the long, continuous archives of climate change that are derived from $\delta^{18}O_p$ variations, such as speleothems, those most useful for paleo-ENSO reconstructions may be those with the most direct climatic interpretations. That is, in locations like those situated in the equatorial Pacific, where simple, highly local $\delta^{18}O$ climate interpretations of archives are likely to be most valid, the convoluting effects of ENSO-like changes, including moisture source regions, may be easier to constrain. However, single site-based reconstructions should not be interpolated to regional or basin-wide scales for reconstructing past ENSO changes. Rather, to determine the spatial fingerprint of ENSO in the past, climatic responses must be synthesized across networks of reconstructions encompassing many sites. In addition, given the complexities of ENSO-phase hydrological expressions under differing boundary conditions, the interpretations of proxy records may benefit from the use of site-specific forward models that explicitly resolve the relevant, local hydrological response to particular ENSO conditions.

5.3. Limitations of This Study

The experiments utilized in this study are useful for revealing the complexity of hydrological responses to ENSO-associated surface temperature forcings. They do, however, include strong, idealized forcings, and we are limited in the conclusions that we can draw for locating proxy locations that are likely to record temporally stable ENSO impacts. Due to the difficulties in evaluating the utility of these experiments for real-world comparison, we considered only changes in the December–January season. Nonetheless, proxies can record signals in other seasons or can integrate annual averages. Ideally, a gridded proxy-based reconstruction of the tropical Pacific during the mid-Holocene would benefit future model-based analyses of changing ENSO-like expressions.

The comparison of the preindustrial and mid-Holocene experiments was conducted to investigate potential changes under differing boundary conditions. We selected the mid-Holocene as this is a well-constrained target for model-based studies [*Schmidt et al.*, 2004], and we applied the same ENSO$_{WARM}$ and ENSO$_{COOL}$ forcings as the preindustrial experiment suite. By applying the same forcings to both the preindustrial and mid-Holocene experiments, we do not suggest that ENSO conditions during these two periods were indistinguishable. We also utilized a model with a relatively coarse horizontal resolution for the model experiments used in this study. Some model studies have demonstrated that precipitation regimes and other aspects of the hydrological cycle can be more realistically represented by models of high spatial resolution [*Hirota et al.*, 2011]. Similarly, explicit model-based assistance in interpreting paleoclimate proxy records of ENSO-like variability would likely benefit for combining multiple isotope-enabled climate models [*Conroy et al.*, 2013].

It is possible that we will only be able to understand long-term changes in ENSO dynamics with models with improved skill in producing physically realistic intrinsic, freely evolving ENSO variability. However, problems have been identified in the capacity of GCMs to capture realistic cloud feedbacks, large-scale circulation patterns, and atmospheric waves that are necessary for elucidating ENSO expressions [*Zhu et al.*, 2007; *Dufresne and Bony*, 2008]. Teleconnections in recent Coupled Model Intercomparison Project 5 (CMIP5) models show variable skill in different regions [*Weare*, 2013]. While models have generally improved compared to earlier versions, models remain most skillful in capturing observed precipitation and temperature anomalies in the tropics than in teleconnected regions. Furthermore, numerous GCMs do not simulate the phase-locking of ENSO to the annual cycle, due to erroneous zonal temperature gradients, coupling strengths, and thermocline depths [*Ham et al.*, 2013].

6. Conclusions

Using the water isotope- and vapor source distribution tracer-enabled GISS ModelE-R, we examined ENSO-like expressions in the hydrological cycle in various regions (eastern, western, central and northwestern Pacific, and eastern China) for multiple model time slices. Overall, these idealized model experiments reveal

hydrological complexity associated with ENSO-like conditions that may impact interpretations of proxy climate records. First, the regionally specific moisture source tracers incorporated into the model show that substantial changes in hydrology occur across the Pacific basin between the forced El Niño-like and La Niña-like events. The application of ENSO$_{COOL}$ forcings in the preindustrial simulation does not produce climatological anomalies that represent the equal but opposite impacts of the ENSO$_{WARM}$ experiment.

Model results also demonstrate potential sensitivity in the interactions between ENSO-like phases and surface boundary conditions. Although the pattern of mid-Holocene changes for the differing ENSO phases are somewhat muted for rainfall amounts and $\delta^{18}O_p$, changes are simulated in other circulation diagnostics in the mid-Holocene experiments, relative to the preindustrial. There are substantial changes in mid-Holocene moisture sources to the analyzed regions and surface wind fields, even in remote areas, which suggest complex interactions of the forced, idealized ENSO-like conditions with model boundary conditions. Overall, the mid-Holocene is characterized by a differing mean state compared to the preindustrial, with the largest difference in boundary conditions relating to orbital forcing. Differing mid-Holocene orbital configurations result in a redistribution of seasonal insolation in the tropics, which impacts surface temperatures, land-sea temperature contrasts, zonal circulation patterns, and wind stress. Although ENSO dynamics and teleconnections are known to be influenced by changes in the large-scale state of the coupled ocean-atmosphere systems and particularly the annual cycle, the assumption of stationarity in climatic relationships between regions and between ENSO phases underpins many paleoclimatic reconstructions.

We suggest that the uncertainty surrounding the nonstationarity of ENSO teleconnections must be explicitly addressed in proxy-based paleo-ENSO reconstructions, particularly as model results demonstrate the potential sensitivity of ENSO-like phase impacts to surface boundary conditions. In particular, the simulations of the preindustrial and mid-Holocene demonstrate complex impacts on various aspects of the hydrological cycle, including moisture source regions, which may be integrated into proxy records (such as $\delta^{18}O$ archives) and hence convolute reconstructions of paleoclimates. Ideally, our further understanding of paleo-ENSO changes will be guided by climatic responses synthesized across networks of reconstructions encompassing many sites, rather than from single sites alone. The synthesis of many sites will allow the spatial fingerprints of ENSO under varying boundary conditions (such as throughout the Holocene) to be determined more robustly and precisely.

The scope of this study has been limited to investigating potential ENSO-like changes in the preindustrial and mid-Holocene time slices using idealized experiments and also been focused on isotopic variability. The experiments utilized here are useful for understanding hydrological responses to ENSO-associated temperature forcings under differing boundary conditions, but we reiterate that they do include strong, idealized forcings. As such, these simulations are limited in providing local-scale information for use in interpreting individual proxy records. Further model-based investigation of long-term ENSO dynamics, ideally using physically realistic freely evolving simulated ENSO variability, would be useful for targeting the location of paleoclimatic reconstructions toward regions with comparatively stable ENSO influences through time. In addition, the future use of multiple isotope-enabled climate models would help in interpreting paleoclimate proxy records of ENSO-like variability.

References

Adler, R. F., et al. (2003), The version-2 global precipitation climatology project (GPCP) monthly precipitation analysis (1979-Present), *J. Hydrometeorol.*, 4, 1147–1167, doi:10.1175/1525-7541(2003)004<1147:tvgpcp>2.0.co;2.

Berger, A., and M. F. Loutre (1991), Insolation values for the climate of the last 10 million years, *Quat. Sci. Rev.*, 10, 297–317, doi:10.1016/0277-3791(91)90033-Q.

Brook, E. J., S. Harder, J. Severinghaus, E. J. Steig, and C. M. Sucher (2000), On the origin and timing of rapid changes in atmospheric methane during the Last Glacial Period, *Global Biogeochem. Cycles*, 14, 559–572, doi:10.1029/1999GB001182.

Brown, J., I. Simmonds, and D. Noone (2006), Modeling $\delta^{18}O$ in tropical precipitation and the surface ocean for present-day climate, *J. Geophys. Res.*, 111, D05105, doi:10.1029/2004JD005611.

Brown, J., M. Collins, A. Tudhope, and T. Toniazzo (2008), Modelling mid-Holocene tropical climate and ENSO variability: Towards constraining predictions of future change with palaeo-data, *Clim. Dyn.*, 30, 19–36, doi:10.1007/s00382-007-0270-9.

Bush, A. B. G. (2007), Extratropical influences on the El-Nino-Southern Oscillation during the Late Quaternary, *J. Clim.*, 20, 788–800, doi:10.1175/JCLI4048.1.

Cai, W., et al. (2014), Increasing frequency of extreme El Nino events due to greenhouse warming, *Nat. Clim. Change*, 4, 111–116, doi:10.1038/nclimate2100.

Chiang, J. C. H., Y. Fang, and P. Chang (2009), Pacific climate change and ENSO activity in the mid-Holocene, *J. Clim.*, 22, 923–939, doi:10.1175/2008JCLI2644.1.

Chou, C., and M.-H. Lo (2007), Asymmetric responses of tropical precipitation during ENSO, *J. Clim.*, 20, 3411–3433, doi:10.1175/jcli4197.1.

Chung, C. T. Y., S. B. Power, J. M. Arblaster, H. A. Rashid, and G. L. Roff (2014), Nonlinear precipitation response to El Niño and global warming in the Indo-Pacific, *Clim. Dyn.*, 42, 1837–1856, doi:10.1007/s00382-013-1892-8.

Clement, A. C., R. Seager, and M. A. Cane (1999), Orbital controls on the El Nino/Southern Oscillation and the tropical climate, *Paleoceanography*, *14*, 441–456, doi:10.1029/1999PA900013.

Cobb, K. M., C. D. Charles, H. Cheng, and R. L. Edwards (2003), El Niño/Southern Oscillation and tropical Pacific climate during the last millennium, *Nature*, *424*, 271–276, doi:10.1038/nature01779.

Cobb, K. M., N. Westphal, H. R. Sayani, J. T. Watson, E. Di Lorenzo, H. Cheng, R. L. Edwards, and C. D. Charles (2013), Highly variable El Niño-Southern Oscillation throughout the Holocene, *Science*, *339*, 67–70, doi:10.1126/science.1228246.

Collins, M., et al. (2010), The impact of global warming on the tropical Pacific Ocean and El Niño, *Nat. Geosci.*, *3*, 391–397, doi:10.1038/ngeo868.

Conroy, J. L., K. M. Cobb, and D. Noone (2013), Comparison of precipitation isotope variability across the tropical Pacific in observations and SWING2 model simulations, *J. Geophys. Res. Atmos.*, *118*, 5867–5892, doi:10.1002/jgrd.50412.

Donders, T. H., F. Wagner-Cremer, and H. Visscher (2008), Integration of proxy data and model scenarios for the mid-Holocene onset of modern ENSO variability, *Quat. Sci. Rev.*, *27*, 571–579, doi:10.1016/j.quascirev.2007.11.01.

Dufresne, J.-L., and S. Bony (2008), An assessment of the primary sources of spread of global warming estimates from coupled atmosphere-ocean models, *J. Clim.*, *21*, 5135–5144, doi:10.1175/2008jcli2239.1.

Emile-Geay, J., K. M. Cobb, M. E. Mann, and A. T. Wittenberg (2012), Estimating central equatorial Pacific SST variability over the past millennium. Part II: Reconstructions and implications, *J. Clim.*, *26*, 2329–2352, doi:10.1175/jcli-d-11-00511.1.

Gallant, A. J. E., S. J. Phipps, D. J. Karoly, A. B. Mullan, and A. M. Lorrey (2013), Nonstationary Australasian teleconnections and implications for paleoclimate reconstructions, *J. Clim.*, *26*, 8827–8849, doi:10.1175/jcli-d-12-00338.1.

Gergis, J. L., K. Braganza, A. Fowler, S. Mooney, and J. Risbey (2006), Reconstructing El Niño–Southern Oscillation (ENSO) from high-resolution palaeoarchives, *J. Quat. Sci.*, *21*, 707–722, doi:10.1002/jqs.1070.

Ham, Y.-G., J.-S. Kug, D. Kim, Y.-H. Kim, and D.-H. Kim (2013), What controls phase-locking of ENSO to boreal winter in coupled GCMs?, *Clim. Dyn.*, *40*, 1551–1568, doi:10.1007/s00382-012-1420-2.

Hansen, J., et al. (2007), Climate simulations for 1880-2003 with GISS modelE, *Clim. Dyn.*, *29*, 661–696, doi:10.1007/s00382-007-0255-8.

Hirota, N., Y. N. Takayabu, M. Watanabe, and M. Kimoto (2011), Precipitation reproducibility over tropical oceans and its relationship to the double ITCZ problem in CMIP3 and MIROC5 climate models, *J. Clim.*, *24*, 4859–4873, doi:10.1175/2011jcli4156.1.

Hoerling, M. P., A. Kumar, and T. Xu (2001), Robustness of the nonlinear climate response to ENSO's extreme phases, *J. Clim.*, *14*, 1277–1293, doi:10.1175/1520-0442(2001)014<1277:rotncr>2.0.co;2.

Indermuhle, A., et al. (1999), Holocene carbon-cycle dynamics based on CO_2 trapped in ice at Taylor Dome, Antarctica, *Nature*, *398*, 121–126, doi:10.1038/18158.

Jones, P. D., and M. E. Mann (2004), Climate over the past millenia, *Rev. Geophys.*, *42*, RG2002, doi:10.1029/2003RG000143.

Kelley, M. (2003), Water tracers and the hydrologic cycle in a GCM, Doctor of Philosophy, Department of Earth and Environmental Sciences, Columbia University, New York.

Koutavas, A., J. Lynch-Stieglitz, T. M. Marchitto Jr., and J. P. Sachs (2002), El Niño-like pattern in ice age tropical Pacific sea surface temperature, *Science*, *297*, 226–230, doi:10.1126/science.1072376.

Lachniet, M. S., S. J. Burns, D. R. Piperno, Y. Asmerom, V. J. Polyak, C. M. Moy, and K. Christenson (2004), A 1500-year El Nino/Southern Oscillation and rainfall history for the Isthmus of Panama from speleothem calcite, *J. Geophys. Res.*, *109*, D20117, doi:10.1029/2004JD004694.

Lea, D. W., D. K. Pak, C. L. Belanger, H. J. Spero, M. A. Hall, and N. J. Shackleton (2006), Paleoclimate history of Galápagos surface waters over the last 135,000 yr, *Quat. Sci. Rev.*, *25*, 1152–1167.

LeGrande, A. N., and G. A. Schmidt (2009), Sources of Holocene variability of oxygen isotopes in paleoclimate archives, *Clim. Past*, *5*, 441–455, doi:10.5194/cp-5-441-2009.

Lewis, S. C., A. N. LeGrande, M. Kelley, and G. A. Schmidt (2010), Water vapour source impacts on oxygen isotope variability in tropical precipitation during Heinrich events, *Clim. Past*, *6*, 325–343, doi:10.5194/cp-6-325-2010.

Lewis, S. C., A. N. LeGrande, M. Kelley, and G. A. Schmidt (2013), Modeling insights into deuterium excess as an indicator of water vapor source conditions, *J. Geophys. Res. Atmos.*, *118*, 243–262, doi:10.1029/2012JD017804.

Luan, Y., P. Braconnot, Y. Yu, W. Zheng, and O. Marti (2012), Early and mid-Holocene climate in the tropical Pacific: Seasonal cycle and interannual variability induced by insolation changes, *Clim. Past*, *8*, 1093–1108, doi:10.5194/cp-8-1093-2012.

McGregor, H. V., M. J. Fischer, M. K. Gagan, D. Fink, S. J. Phipps, H. Wong, and C. D. Woodroffe (2013a), A weak El Nino/Southern Oscillation with delayed seasonal growth around 4,300 years ago, *Nat. Geosci.*, *6*, 949–953, doi:10.1038/ngeo1936.

McGregor, S., N. Ramesh, P. Spence, M. H. England, M. J. McPhaden, and A. Santoso (2013b), Meridional movement of wind anomalies during ENSO events and their role in event termination, *Geophys. Res. Lett.*, *40*, 749–754, doi:10.1002/grl.50136.

Meehl, G. A., P. R. Gent, J. M. Arblaster, B. L. Otto-Bliesner, E. C. Brady, and A. Craig (2001), Factors that affect the amplitude of El Niño in global coupled climate models, *Clim. Dyn.*, *17*, 515–526, doi:10.1038/nature01194.

Morice, C. P., J. J. Kennedy, N. A. Rayner, and P. D. Jones (2012), Quantifying uncertainties in global and regional temperature change using an ensemble of observational estimates: The HadCRUT4 data set, *J. Geophys. Res.*, *117*, D08101, doi:10.1029/2011JD017187.

Power, S., M. Haylock, R. Colman, and X. Wang (2006), The predictability of interdecadal changes in ENSO activity and ENSO teleconnections, *J. Clim.*, *19*, 4755–4771, doi:10.1175/jcli3868.1.

Power, S., F. Delage, C. Chung, G. Kociuba, and K. Keay (2013), Robust twenty-first-century projections of El Niño and related precipitation variability, *Nature*, *502*, 541–545, doi:10.1038/nature12580.

Reynolds, R. W., and T. M. Smith (1994), Improved global sea surface temperature analyses using optimum interpolation, *J. Clim.*, *7*, 929–948, doi:10.1175/1520-0442(1994)007<0929:IGSSTA>2.0.CO;2.

Rosenthal, Y., and A. J. Broccoli (2004), In search of paleo-ENSO, *Science*, *304*, 219–221.

Rozanski, K., L. Araguas-Araguas, and R. Gonfiantini (1993), Isotopic patterns in modern global precipitation, in *Climate Change in Continental Isotopic Records*, *Geophys. Monogr.*, vol. 78, edited by P. K. Swart et al., pp. 1–36, AGU, Washington, D. C.

Schmidt, G. A., D. T. Shindell, R. L. Miller, M. E. Mann, and D. Rind (2004), General circulation modelling of Holocene climate variability, *Quat. Sci. Rev.*, *23*, 2167–2181, doi:10.1016/j.quascirev.2004.08.005.

Schmidt, G. A., G. Hoffmann, D. T. Shindell, and Y. Y. Hu (2005), Modeling atmospheric stable water isotopes and the potential for constraining cloud processes and stratosphere-troposphere water exchange, *J. Geophys. Res.*, *110*, D21314, doi:10.1029/2005JD005790.

Schmidt, G. A., et al. (2006), Present-day atmospheric simulations using GISS ModelE: Comparison to in situ, satellite, and reanalysis data, *J. Clim.*, *19*, 153–192, doi:10.1175/JCLI3612.1.

Schmidt, G. A., A. N. LeGrande, and G. Hoffmann (2007), Water isotope expressions of intrinsic and forced variability in a coupled ocean-atmosphere model, *J. Geophys. Res.*, *112*, D10103, doi:10.1029/2006JD007781.

Shulmeister, J., D. T. Rodbell, M. K. Gagan, and G. O. Seltzer (2006), Inter-hemispheric linkages in climate change: Paleo-perspectives for future climate change, *Clim. Past*, *2*, 79–122, doi:10.5194/cp-2-167-2006.

Sowers, T., R. B. Alley, and J. Jubenville (2003), Ice core records of atmospheric N₂O covering the last 106,000 years, *Science*, *301*, 945–948, doi:10.1126/science.108529.

Tindall, J. C., P. J. Valdes, and L. C. Sime (2009), Stable water isotopes in HadCM3: Isotopic signature of El Niño-Southern Oscillation and the tropical amount effect, *J. Geophys. Res.*, *114*, D04111, doi:10.1029/2008JD010825.

Toniazzo, T. (2006), Properties of El Niño-Southern Oscillation in different equilibrium climates with HadCM3, *J. Clim.*, *19*, 4854–4876.

Tudhope, A. W., C. P. Chilcott, M. T. McCulloch, E. R. Cook, J. Chappell, R. M. Ellam, D. W. Lea, J. M. Lough, and G. B. Shimmield (2001), Variability in the El Niño-Southern Oscillation through a glacial-interglacial cycle, *Science*, *291*, 1511–1517, doi:10.1126/science.1057969.

Vuille, M., and M. Werner (2005), Stable isotopes in precipitation recording South American summer monsoon and ENSO variability: Observations and model results, *Clim. Dyn.*, *25*, 401–413, doi:10.1007/s00382-005-0049-9.

Vuille, M., R. S. Bradley, M. Werner, R. Healy, and F. Keimig (2003), Modeling δ¹⁸O in precipitation over the tropical Americas: 1. Interannual variability and climatic controls, *J. Geophys. Res.*, *108*(D6), 4174, doi:10.1029/2001JD002038.

Weare, B. (2013), El Niño teleconnections in CMIP5 models, *Clim. Dyn.*, *41*, 2165–2177, doi:10.1007/s00382-012-1537-3.

Wilson, R., C. Edward, D. A. Rosanne, R. Nadja, N. E. Michael, T. Alexander, and A. Rob (2010), Reconstructing ENSO: The influence of method, proxy data, climate forcing and teleconnections, *J. Quat. Sci.*, *25*, 62–78, doi:10.1002/jqs.1297.

Wittenberg, A. T. (2004), Extended wind stress analyses for ENSO, *J. Clim.*, *17*(13), 2526–2540.

Zhu, P., J. J. Hack, and J. T. Kiehl (2007), Diagnosing cloud feedbacks in general circulation models, *J. Clim.*, *20*, 2602–2622, doi:10.1175/jcli4140.1.